Controllable construction of CoP nanoparticles anchored on a nitrogen-doped porous carbon as an electrocatalyst for highly efficient oxygen reduction in Zn-air batteries

YAN Xiao-li[1,*], WANG Kui[1], HAO Shu-wei[2], ZHOU Guang-da[1],
YANG Hao-wei[1], ZHANG Hua[1], GUO Jun-jie[1,*]

（1. *Key Laboratory of Interface Science and Engineering in Advanced Materials*, *Ministry of Education*, *College of Materials Science and Engineering*, *Taiyuan University of Technology*, *Taiyuan* 030024, *China*;
2. *College of Materials Science and Engineering*, *Huaqiao University*, *Xiamen* 361021, *China*）

Abstract： Exploring cost-efficient and highly-efficient noble metal-free catalysts for the oxygen reduction reactions (ORRs) involved in sustainable energy devices remains a great challenge. Transition-metal phosphides supported on heteroatom-doped carbons have shown potential as alternative candidates for precious metals because of their tunable electronic structures and higher catalytic performance. Phosphating was used to construct CoP nanoparticles (NPs) anchored on a nitrogen-doped porous carbon framework (CoP@NC) from Co NPs loaded on NC, using PH_3 gas released from NaH_2PO_2 during heat treatment. The dodecahedral structure of Co NPs was retained in their transformation to CoP NPs. The CoP@NC electrocatalyst shows a remarkable ORR activity with a half-wave potential up to 0.92 V under alkaline conditions, which is attributed to the combined coupling between the well dispersed CoP nanoparticles on the nitrogen-doped carbon and the efficient mass transport in the porous structure. Zinc-air batteries assembled with the CoP@NC electrocatalyst as a cathode have a high open-circuit voltage of 1.51 V and power density of 210.1 mW cm^{-2}. This work provides a novel strategy to develop low-cost catalysts with an excellent ORR performance to promote their practical use in metal-air batteries.

Key words: Electrocatalysts; Co-based catalysts; Metal phosphides; ORR; Zinc-air battery

1 Introduction

The oxygen reduction reaction (ORR) is a key cathodic reaction in next-generation renewable energy conversion devices such as metal-air batteries[1–4]. However, the main challenge ORR face is lacking excellent catalysts, mainly due to the high energy barriers and sluggish kinetics caused by the four-electron/proton transfer pathway and intermediates adsorption/desorption in ORR[5–8]. Current commercially available platinum (Pt)-based catalysts hinder the large-scale and sustainable application of these devices by their low natural abundance, high-cost, and poor durability[2,9,10]. Therefore, the researchers focused their efforts on cost-effective precious-metal-free ORR catalysts to promote the commercial application of clean-energy devices [11–14].

Among various alternatives of Pt-based electrocatalysts, transition-metal phosphide (TMP) catalysts have attracted extensive interests due to their good conductivity, excellent stability, adjustable electronic structures and abundant bonding types[15–18]. Recent studies have shown that the synergy between the various active components can improve the catalytic activity of TMP catalysts[19–24]. For example, a composite of Co_2P nanoparticle decorated N, P co-doped defective carbon materials (Co_2P@CoNPG) exhibits excellent catalytic activity attributed to the synergistic effects of Co_2P and Co-N_x active sites[25–29]. In addition, the powerful synergistic coupling between phosphides and defect-abundant carbon matrix can also enhance the catalytic activity of TMP catalysts[30]. CoP particles loaded on N, P-doped necklace-like carbon show excellent ORR activity due to the synergistic ef-

Received date: 2024-01-11； **Revised date:** 2024-03-28

Corresponding author: YAN Xiao-li, Lecturer. E-mail: yanxiaoli@tyut.edu.cn;
GUO Jun-jie, Professor. E-mail: guojunjie@tyut.edu.cn

Supplementary data associated with this article can be found in the online version.

fects between CoP nanoparticles and carbon matrix[31]. Moreover, encapsulation of TMPs into carbon materials has been proved to further boost electrocatalytic activity and prevent the chemical corrosion[32–35]. Li et al. prepared a multifunctional Co-NC@CoP-NC catalyst, and its better ORR performance and stability are due to the high efficient of CoP and the complete protection of cobalt by the nitrogen-doped carbon layer [19]. Nevertheless, it has been reported that different crystalline phases (CoP and Co_2P) of cobalt phosphide exist in TMP catalysts, which show different catalytic preferences for different catalytic reactions. Scott M. Geyer et al. compared the catalytic performance of well-dispersed CoP and Co_2P nanocrystals, confirming that Co_2P is preferred species for oxygen evolution reaction (OER) due to the easy formation of abundant Co_2P@COOH heterogeneous structures and CoP for ORR due to abundant P sites[36]. Therefore, effective and versatile synthetic methodology for the controllable fabrication of TMP catalysts should make full use of the advantages of structural and compositional properties to maximize the ORR performance.

In this work, a high-efficient CoP@NC catalyst (CoP nanoparticles wrapped by nitrogen-doped carbon shells supported on hierarchical porous carbon framework) was successfully achieved by taking advantage of the excellent properties of metal phosphide materials and the unique advantages of ZIF-based porous structures with a reasonable microporous/mesoporous ratio synthesized in our previous paper[37]. The prepared CoP@NC catalyst exhibited boosted ORR activity under alkaline conditions. The zinc-air batteries assembled using the CoP@NC electrocatalyst also demonstrated good performance with a peak power density up to 210.1 mW cm^{-2} and long durability.

2 Experiment

2.1 Materials

Zinc (Ⅱ) acetylacetonate ($Zn(acac)_2$, 98%), Cobaltous nitrate hexahydrate ($Co(NO_3)_2·6H_2O$, 98%), 2-methylimidazole (2-MeIM, 98%), 1,10-phenanthroline (phen, 98%), sodium hypophosphite (NaH_2PO_2, 98%) were provided from Shanghai Aladdin Company. 20% Pt/C was purchased from Johnson Matthey. All chemical reagents purchased for the experiment were used directly without any treatment.

2.2 Catalyst preparation

2.2.1 Preparation of $Zn(acac)_2$-0.4@ZIF-67

$Zn(acac)_2$-0.4@ZIF-67 was synthesized according to the previous method of our team[37]. First, 5 mmol of $Co(NO_3)_2·6H_2O$ was dissolved in 50 mL of methanol and mixed well by sonication. Subsequently, 2 mmol of $Zn(acac)_2$ and 1 mmol of 1,10-phenanthroline were added to the above solution and stirred magnetically to dissolve them completely. Lastly, the above mixed solution was rapidly added to 50 mL of methanol solution containing 30 mmol of 2-methylimidazole, and the mixture was completely dissolved by magnetic stirring. The well-mixed solution was poured into a 50 mL in Teflon reactor. The reaction was then carried out hydrothermally in a desiccator for 4 h at a reaction temperature of 120 °C. $Zn(acac)_2$-0.4@ZIF-67 powder was obtained through centrifugation, rinsed twice with methanol and heated at 60 °C overnight in vacuum environment to obtain dry a sample.

2.2.2 Preparation of Co@NC

The produced sample was placed in a crucible and then heated in a tube furnace vented with nitrogen. The heating temperature was gradually increased to 900 °C and maintained 2 h. The ramping rate of temperature was 5 °C·min^{-1}.

2.2.3 Preparation of CoP@NC

The above synthesized Co@NC powder and NaH_2PO_2 powder were ground and stirred at room temperature to explore the optimal phosphorus doping conditions. Subsequently, they were placed in a tube furnace ventilated with N_2 at 350 °C for 2 h, and then cooled naturally at room temperature. Finally, CoP@NC catalyst were obtained.

2.3 Characterization

The morphology and microstructure of the produced material were studied using JEOL JEM-2010 transmission electron microscope (TEM). TESCAN LYRA3-XMH scanning electron microscope (SEM)

equipped with the energy-dispersive X-ray spectrum (EDS) was used to gain the catalyst morphology images and elemental mapping. The crystal structures of the sample were determined using Cu *K*α radiation X-ray diffraction (XRD) (Rigaku). The Escalab 250X X-ray photoelectron spectroscopy (XPS) instrument was adopted to determine the elements and valence state of the produced samples.

2.4 Electrochemical measurements

To ascertain the electrochemical characteristics for each sample obtained for the oxygen reduction performance, three electrodes located on the CHI Electrochemical Station (760E) was utilized. The working electrode in this experiment was the glass carbon disc electrode coated (RDE, 5.6 mm diameter) with an as-prepared catalyst, the reference electrode used in measurement was a saturated calomel electrode, while the counter electrode was a graphene rod electrode. To prepare a well-dispersed catalyst ink, 0.38 mL of a mixture of ethanol and deionized water (1 ∶ 1) was added to an vial containing 20 mg of CoP@NC and sonicated for 30 min. Next, 20 μL of 5% Nafion (DuPont) film-forming agent was added to the dispersed homogeneous ink and sonication was continued for 30 min. Then, 10 μL of the above-prepared dispersion was rapidly dripped onto the working electrode and dried naturally in air. Linear scanning voltammetry (LSV) curves were obtained in the O_2-saturated electrolyte by setting the scanning rate to 5 mV s^{-1} and the working electrode speed to 1 600 r min^{-1}. The potentials measured under the above experimental conditions all need to be modified to reversible hydrogen electrodes (RHE) according to Eq. (1):

$$E(v\text{s. RHE}) = E(v\text{s. SCE}) + 0.2438 + 0.0592 \times \text{pH} \quad (1)$$

The number of electron transfer (n) in the reaction can be estimated by fitting the Koutecky-Levich (K-L) formula to the LSV obtained at different rotational speeds, according to Eq. (2) and (3):

$$\frac{1}{J} = \frac{1}{J_L} + \frac{1}{J_K} = \frac{1}{B\omega^{1/2}} + \frac{1}{J_K} \quad (2)$$

$$B = 0.62nFC_0D_0^{2/3}v^{-1/6} \quad (3)$$

The yield of H_2O_2 and electron transfer number (n) during ORR were measured by the rotating ring disk electrode (RRDE), according to Eq. (4) and (5):

$$H_2O_2\% = \frac{200I_r}{I_r + (I_r/N)} \quad (4)$$

$$n = 4 \times \frac{I_d}{I_d + (I_r/N)} \quad (5)$$

In the formula, I_r and I_d is the disk and ring current, respectively. N (0.37) is the current efficiency of Pt ring.

2.5 Alkaline zinc-air battery test

Using a homemade electrochemical cell, the electrocatalytic performance of the produced catalyst was examined in a rechargeable Zn-air battery. Herein, a zinc plate (0.3 mm), a catalyst supported by carbon cloth, and 6 mol L^{-1} KOH with 0.2 mol L^{-1} $Zn(OAc)_2$ solution as the anode, air cathode, and electrolyte, respectively, were used to create a handmade rechargeable ZAB. Using a spraying technique, the air electrode was made, and the carbon fiber paper was coated with the CoP@NC catalyst with a loading of 1.0 mg cm^{-2}. By depleting the characteristics of zinc flake, the energy density and specific capacity may be calculated. The voltage-current polarization of batteries was performed on a CHI 760E electrochemical workstation. A Neware Battery Test Station System (CT-4008T) was used to conduct the discharge-charge at 10 mA cm^{-2}.

3 Results and discussion

3.1 Microstructure analysis

TMPs exhibit excellent stability and ORR activity. Therefore, we expect to convert the Co particles in the hierarchical porous nitrogen-doped carbon framework into CoP nanoparticles for highly efficient and stable ORR. The simple synthesis procedure of the CoP@NC based on the ZIF-67 precursor is shown in Scheme 1. Firstly, the Co@NC catalyst with reasonable size and micropore/mesopore ratio was synthesized by high temperature pyrolysis. Then, Co@NC and NaH_2PO_2 were mixed well in a mortar, and secondary pyrolysis was carried out at 350 °C to obtain the CoP@NC catalyst. During the secondary pyrolysis, NaH_2PO_2 can be decomposed at 300 °C to gener-

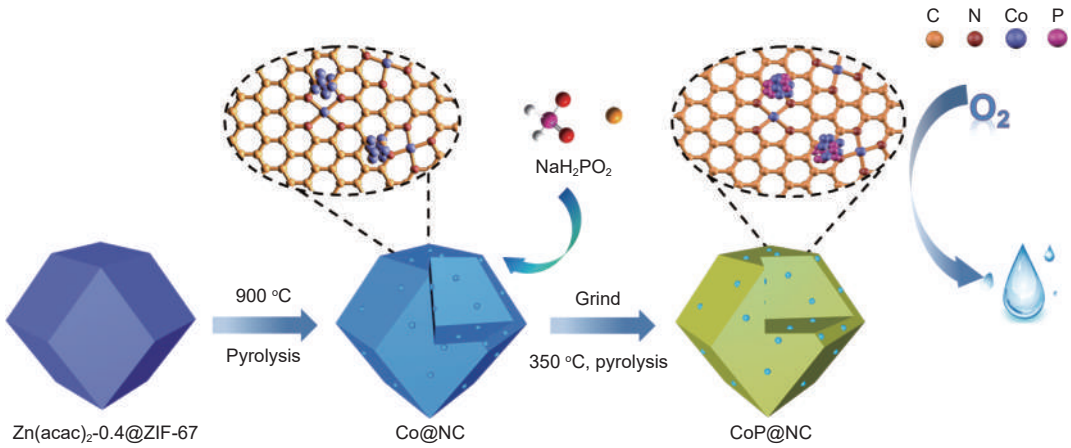

Scheme 1　Fabrication schematic of CoP@NC

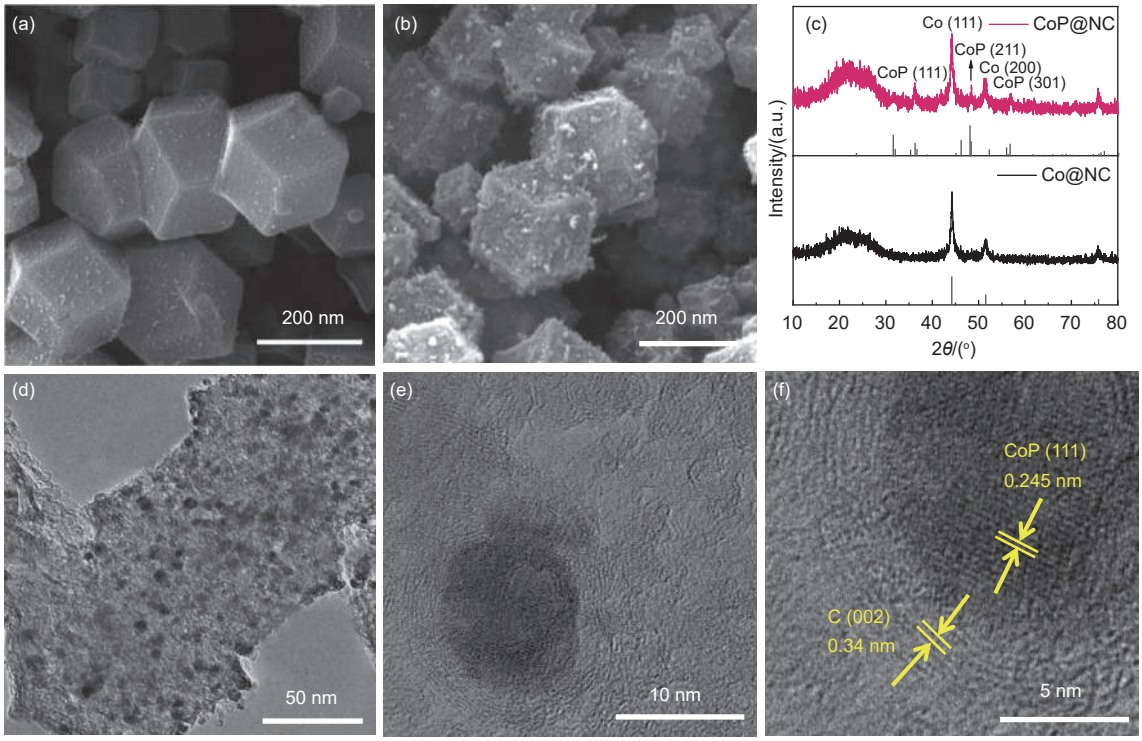

Fig. 1　SEM micrographs of (a) Co@NC[37] and (b) CoP@NC electrocatalysts. (c) Corresponding XRD patterns. (d-f) TEM images of CoP@NC catalyst

ate PH_3 gas, which can phosphorylate Co to form CoP nanoparticles in situ without changing the dodecahedral structure of the carrier.

Fig. 1a and b indicates the SEM micrographs of Co@NC and CoP@NC. Numerous small Co or CoP particles are dispersed evenly on the porous carbon framework without obvious agglomeration. The Co@NC catalyst synthesized before phosphorylation shows a 3D rhombic dodecahedral structure with smooth surface and right-angle edges in Fig. 1a. From Fig. 1b, it can be found that the CoP@NC still maintains its original polyhedral structure after phosphorylation to some extent. However, its surface becomes much rougher in comparison to Co@NC catalyst and presents many folds, which may increase its surface area, thereby increasing the catalytically active area of the catalyst. Moreover, the porous structure of the ZIF-derived carbon framework was improved by pre-adjusting the ratio of zinc/cobalt ions, which effectively accommodated and exposed more active sites. As can be seen from Fig. S1, the phosphorylation process extends more carbon nanotube

structure on the catalyst surface, further increasing the catalytic active area and electrical conductivity. The good dodecahedral structure, appropriate pore distribution and the extended carbon nanotube structure jointly promote the mass transfer and electron transfer during the catalytic reaction, which effectively improves the ORR catalytic activity of CoP@NC.

The crystalline phase structures of CoP@NC and Co@NC were studied by XRD (Fig. 1c). The distinctive wide diffraction peaks at 23.5°, 31.6°, 36.4°, 46.1°, 48.3° and 56.7° of CoP@NC are well consistent with the (101), (002), (111), (112), (211) and (301) planes of standard CoP, respectively (JCPDS #29-0497)[38,39]. The distinctive wide diffraction peaks at 44.3°, 51.6° and 76.2° demonstrate the existence of Co, which agrees closely with the pattern of Co@NC (bottom) in Fig. 1c. The peak at 25° is indexed to the (002) graphitic carbon plane (JCPDS#26-1076). The results demonstrate that the Co nanoparticles are successfully phosphorized to form CoP nanoparticles by thermal phosphating under the NaH_2PO_2-generated PH_3 gas and the CoP nanoparticles are evenly embedded into the porous carbon framework.

The actual shape and particle size distribution of CoP@NC were analyzed by TEM. It is a regular rhombic dodecahedral structure with uniform size distribution of about 200 nm (Fig. 1d). Notably, CoP nanoparticles of size around 8 nm are dispersed in the carbon framework (Fig. 1e). High resolution TEM (HR-TEM) image of the CoP@NC exhibits the marked lattice spacing of 0.25 and 0.34 nm, which were indexed to the CoP (111) plane and graphitic carbon (002) plane, respectively (Fig. 1f). These results demonstrate that the CoP nanoparticles are wrapped by N-doped carbon shells, both of which are supported on porous carbon framework. Combined with the morphology of the Co@NC catalysts (detailed discuss in our previous study[37]), it is found that the in-situ phosphating process converts Co nanoparticles to CoP, which maintains the porous structure of carbon framework and guarantees enough active sites for electrochemical reactions. Additionally, the CoP nanoparticles are protected from aggregation and chemical corrosion by the encapsulated structure, which can boost the activity and stability of the catalyst. Subsequently, to show the elemental distribution of the CoP@NC sample, we tested the EDS elemental mapping images (Fig. S2), which show that N, P and Co elements are evenly dispersed throughout the carbon frameworks.

The elemental composition and electronic valence of Co@NC and CoP@NC were analyzed by XPS. The C, N, O and Co element coexist in the full XPS surveys of these electrocatalysts (Fig. S3). Evidently, CoP@NC shows an additional P 2p peak at around 130 eV, demonstrating the successful doping of phosphorus[40]. The peaks at 284.6, 285.4, 286.9 and 289.2 eV in C 1s spectrum correspond to C—C, C—N, C—O/C—P and O=C—O, respectively (Fig. 2a). The N 1s spectrum of CoP@NC electrocatalyst has 5 peaks at 398.1, 399.1, 400.2, 401.1 and 403.9 eV, corresponding to pyridine-N, Co-N_x, pyrrole-N, graphite-N and oxidized-N peaks, respectively (Fig. 2b). The presence of pyridine-N, Co-N_x and graphite-N can not only contribute to the ORR performance, but also demonstrate the nitrogen species are successful bonded to the supporter[41–43]. According to the Co 2p spectrum (Fig. 2c), the peaks of Co $2p_{3/2}$ at 778.4 and 781.1 eV for the CoP@NC electrocatalyst are linked to Co—P and Co—O, respectively. The presence of Co—P species indicates the CoP is formed in the carbon frameworks. The peaks observed at 793.3 and 797.2 eV are linked to Co $2p_{1/2}$. Moreover, two distinct peaks at 785.6 and 802.6 eV are ascribed to satellite peaks caused by the spin-orbit coupling of Co^{2+}. In addition, the peak corresponding to Co^0 disappears, further demonstrating the conversion of Co to CoP in the carbon shell. The P 2p spectrogram of the CoP@NC electrocatalyst has 4 peaks (Fig. 2d). The two fitted peaks at 129.5, 130.3 eV correspond to the P $2p_{3/2}$ and the P $2p_{1/2}$ in Co—P, respectively. Additionally, the fitted peak at 133.9 eV can be correlated to P—O, which is probably a P species produced by surface oxidation from exposure to air. Meanwhile, the high-resolution P 2p XPS spectrum (Fig. 2d) of CoP@NC reveals the presence of

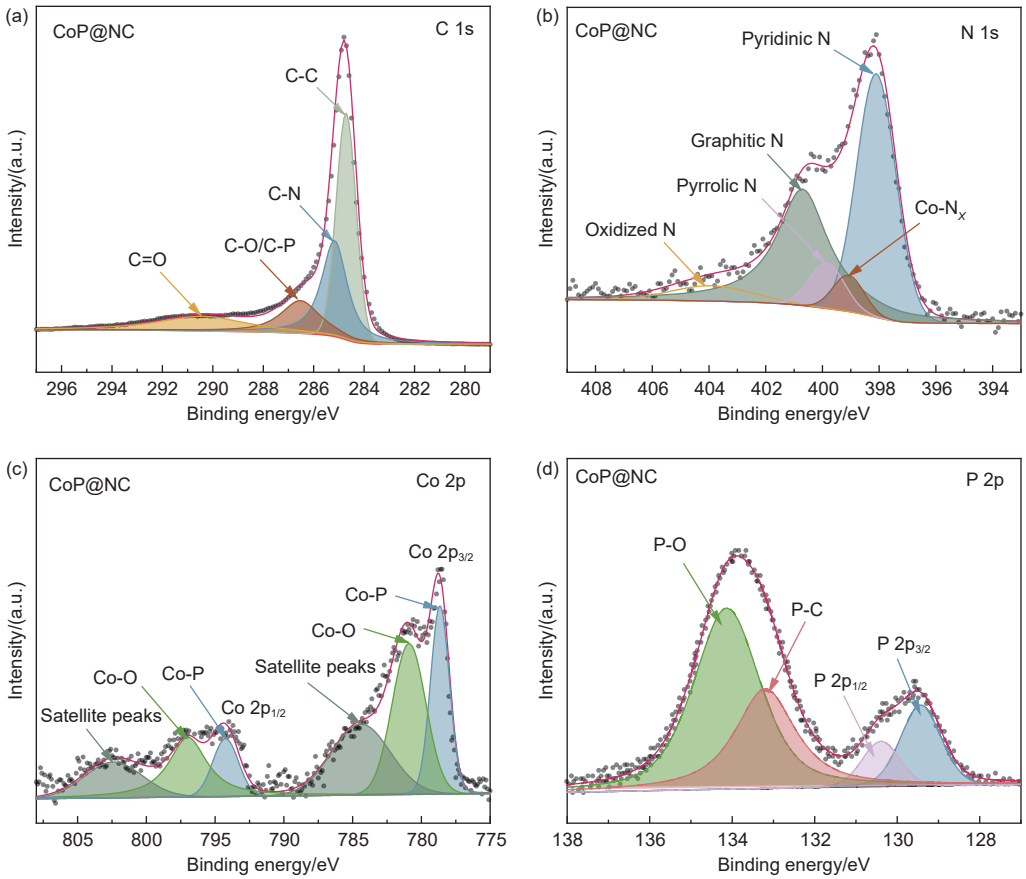

Fig. 2　High-resolution deconvoluted XPS analysis of (a) C 1s, (b) N 1s, (c) Co 2p and (d) P 2p

P—C (132.6 eV). These results indicate that the phosphorus was successfully doped into the porous carbon framework. The phosphating treatment forms the CoP active site and introduces P atoms with high electronegativity into the carbon framework. This can modulate the electronic structure of the monatomic metal Co site through the proximity or remote coordination effect, reducing the energy barrier of the intermediate product and optimizing the ORR catalytic ability of the catalyst.

3.2　ORR catalyst activity

To verify the electrocatalytic activity of CoP@NC towards ORR, cyclic voltammetry (CV) curves of Co@NC, Co@NC, and Pt/C catalysts were determined in alkaline electrolyte solutions saturated with O_2 and N_2 (Fig. S4). All catalysts show a clear oxygen reduction peak in the O_2-saturated solution, but not in the N_2 electrolyte, indicating that all of these catalysts are electrochemically active. Furthermore, it is evident that the cathodic ORR peaks of the various catalysts exhibit distinct positions in the CV curves obtained under O_2-saturated conditions. The CoP@NC displays the most positive redox peak position (Fig. S4) indicating its superior ORR activity compared to CoP@NC and Pt/C catalysts. The speed of the disc electrode was set to 1 600 r min^{-1}, and the LSV curves of all the samples experimentally were obtained at a scan rate of 5 mV·s^{-1} to investigate the ORR catalytic ability of the samples in detail (Fig 3a). The half-wave potential ($E_{1/2}$) and kinetic current density (J_k) of CoP@NC catalysts are compared with the performance of CoP@NC and Pt/C catalysts in Fig. 3b. CoP@NC has the best half-wave potential of 0.92 V, which is higher than that of Co@NC ($E_{1/2}$ of 0.91 V) and Pt/C ($E_{1/2}$ of 0.86 V). Meanwhile, the J_k of CoP@NC reaches a largest value of 16.53 mA cm^{-2} compared to the J_k of Co@NC (15.34 mA cm^{-2}) and Pt/C (6.17 mA cm^{-2}), exhibiting the quick ORR reaction kinetic processs and outstanding ORR electrocatalytic performance of CoP@NC. Tafel slopes were utilized to examine the kinetic behavior of catalysts in the ORR reaction. The Tafel slopes

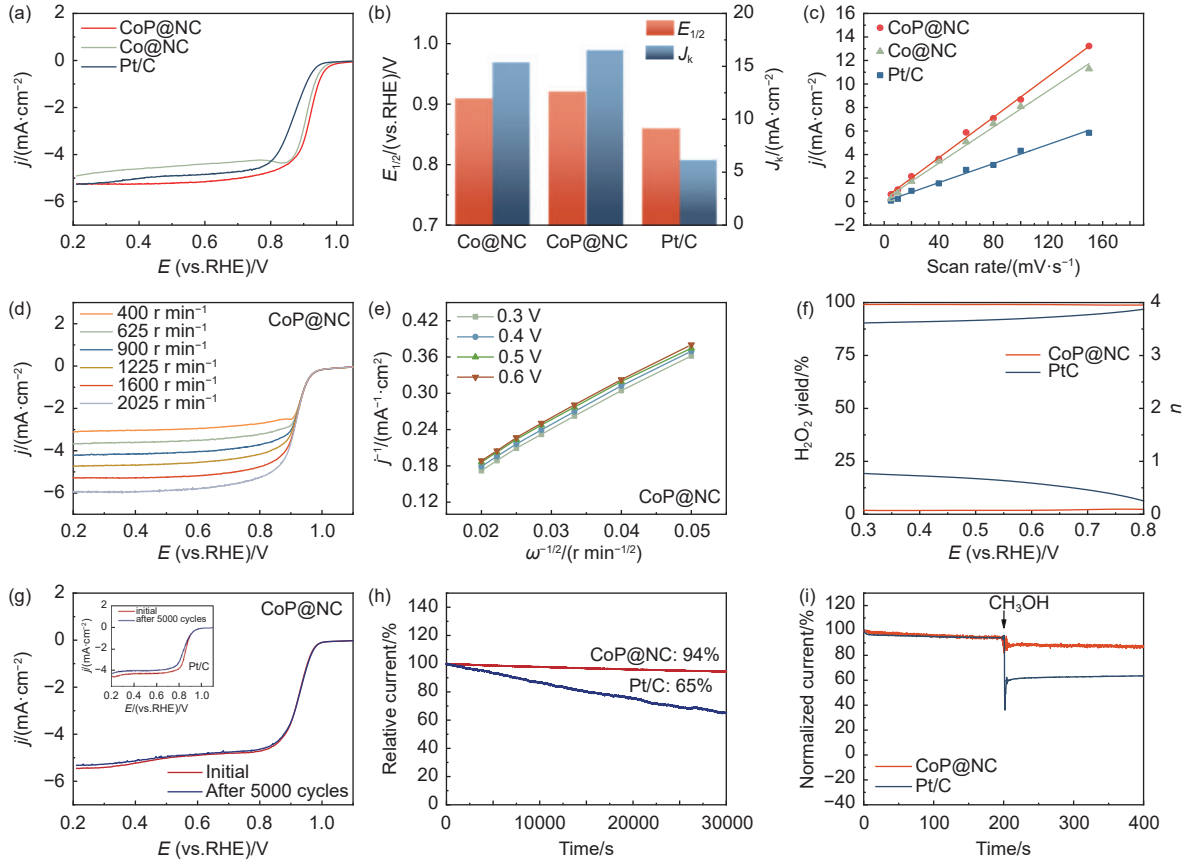

Fig. 3 (a) LSV curves of CoP@NC, Co@NC and Pt/C catalysts. (b) $E_{1/2}$ and J_k (0.85 V) of different catalysts. (c) C_{dl} values of each catalyst versus the scanning speed, and the results are drawn as shown. (d) LSV curves of CoP@NC obtained at rotational speeds of 400-2025 r min^{-1}. (e) K-L plots of CoP@NC. (f) The electron transfer number (n) and the H_2O_2 selectivity of the CoP@NC and Pt/C catalysts measured according to RRDE. (g) LSV curves before and after 5 000 potentiostatic cycles of CoP@NC and Pt/C. (h) Chronoamperometric tests of CoP@NC and Pt/C catalys at 0.60 V (vs. RHE). (i) Methanol antitoxicity testing of CoP@NC and Pt/C catalysts

of the CoP@NC, Co@NC, and Pt/C catalysts with values of 50, 54 and 72 mV dec^{-1}, respectively, are displayed in Fig. S5. The reaction's kinetic characteristics is improved with a smaller Tafel slope[44]. As a result, the CoP@NC electrocatalyst exhibits the lowest Tafel slope, further demonstrating its superior ORR activity. In particular, the prepared CoP@NC catalyst exhibits significant half-wave potentials and relatively low Tafel slopes compared to similar catalysts using CoP as the main active site, further suggesting its superior performance (Table S1).

As shown in Fig. 3c, the electrochemical double layer capacitance values (C_{dl}) obtained during electrochemical experiments were used to calculate the electrochemically active surface area (ECSA). Testing at different scanning speeds produced the CV curves of Faraday zone, and linear fitting of the CV curves produced the C_{dl} values for each catalyst (Fig. S6a-c). From the linear fit curves in Fig. 3c, the C_{dl} value of CoP@NC reaches 86 mF cm^{-2}, better than other catalysts. This implies that the CoP@NC electrocatalyst gives the active site a sizable electrochemically active surface area, facilitating the transfer of active species during ORR. Therefore, in order to illustrate additional electrochemical properties of the CoP@NC electrocatalyst, more detailed tests were carried out.

To evaluate the ORR pathway for CoP@NC, the electrocatalytic kinetics of the catalyst was determined from the LSV polarization curves (Fig. 3d). As the rotational speed increases, the current density exhibits a smooth growth characteristic, indicating that the diffusion distance between oxygen and electrolyte is shortened at high speeds. The K-L plots derived from the linear voltammetric curves at speeds of 400-2025 r min^{-1} show well fitted parallel lines (Fig. 3e), suggesting that CoP@NC catalyst obeys the first-or-

der ORR reaction kinetics[45,46]. The CoP@NC catalyst was subjected to RRDE test to surmise the electron transfer pathway and catalytic reaction efficiency of the catalyst, and obtain the electron transfer number (n) and the by-product hydrogen peroxide yield (H_2O_2%) of CoP@NC in alkaline solution. Fig. 3f shows that the CoP@NC catalyst possesses a better electron transfer number of 3.98 than the commercial Pt/C catalyst over the electrode potential from 0.3 to 0.8 V, while the H_2O_2 yield remains below 2% and is also lower than the Pt/C catalyst (14%). Such results directly confirm that the CoP@NC catalyst maintains excellent 4-electron processes in the ORR. The long-term stability of the catalyst is a good indicator of catalytic life. After 5 000 cycles of the accelerated durability test (ADT), the $E_{1/2}$ of the Pt/C catalyst declines by 15 mV (inset of Fig. 3g), much more than that of CoP@NC catalyst (5 mV) (Fig. 3g). As seen from the i-t plots (Fig. 3h), the current retention rate of the CoP@NC electrocatalyst can still maintain 94% of its initial value after 30 000 s of continuous operation, whereas Pt/C can only maintain 65% of initial current, implying the outstanding long-term stability of CoP@NC. The resistance of the catalyst to methanol toxicity was tested by adding a certain amount of methanol to the electrolyte during chronoamperometric test. Fig. 3i demonstrates that after adding 5 mL of methanol, the current density of CoP@NC fluctuates slightly and then remains stable, while Pt/C shows a significant decline. It shows that CoP@NC catalyst has strong poisoning resistance, which is favorable for practical commercial fuel cell applications.

In summary, CoP@NC electrocatalyst exhibits excellent ORR activity, mainly due to the following reasons: (1) When the N-doped carbon framework with moderate size and reasonable microporous/mesoporous ratio is used as a carrier, its outstanding electrical conductivity facilitates electron transfer and reactant migration during the ORR, which enhances electron/proton transport. (2) Due to the negatively charged P atoms in CoP nanoparticles, the highly graphitized carbon layer is positively charged, the density of states of the Co atom is optimized, which promotes the intermediate adsorption and thus accelerates the ORR. (3) CoP nanoparticles are encapsulated by carbon matrix, which suppresses the chemical corrosion of the CoP nanoparticles and thus improve the stability of the CoP@NC catalyst. (4) The strong electronic coupling between the reasonably porous carbon framework and the highly active sites of CoP nanoparticles is the main reason for the excellent ORR performance.

3.3 Zinc-air battery performance

Zinc-air batteries (ZABs) were constructed using commercial Pt/C and CoP@NC electrocatalysts as air cathode catalysts and zinc plates as anodes, with the aim to investigate their practical applications in the energy conversion device. Compared with Pt/C (1.46 V), ZAB assembled with CoP@NC as an air cathode delivers a high open-circuit voltage up to 1.51 V and presents a high stability and non-decaying state (Fig. 4a). In addition, we connected two CoP@NC based ZABs and successfully lit up the LED panels, proving that they have sufficient power for practical use and broad application prospects (Fig. 4a). As shown in Fig. 4b, the CoP@NC based ZAB has a better discharge polarization curve and peak power density, and the the peak power density of CoP@NC is significantly improved to 210.1 mW cm^{-2} compared to the 143.1 mW cm^{-2} of the Pt/C. Fig. 4c shows that the specific capacitances of CoP@NC and Pt/C based ZABs are 830 and 611 mAh g^{-1}, respectively. Furthermore, as seen in Fig. 4d, the CoP@NC based ZAB shows excellent rate performance at different current densities and maintains a stable voltage at each current density from 2 to 20 mA cm^{-2}, showing a stability superior to that of the Pt/C. In Fig. 4e, the charging/discharging cycle curves of CoP@NC keep stable for 110 h, with a slight increase of 0.2 V in the voltage gap. This result reveals the excellent recharge ability and outstanding long-term durability of the CoP@NC based ZAB under high charging potential during repeated charge/discharge. Summarizing the ZAB performance parameters of CoP@NC and other advanced catalysts, it is clear that the assembled ZAB based on CoP@NC outperforms most other catalysts (Table S2). These performance

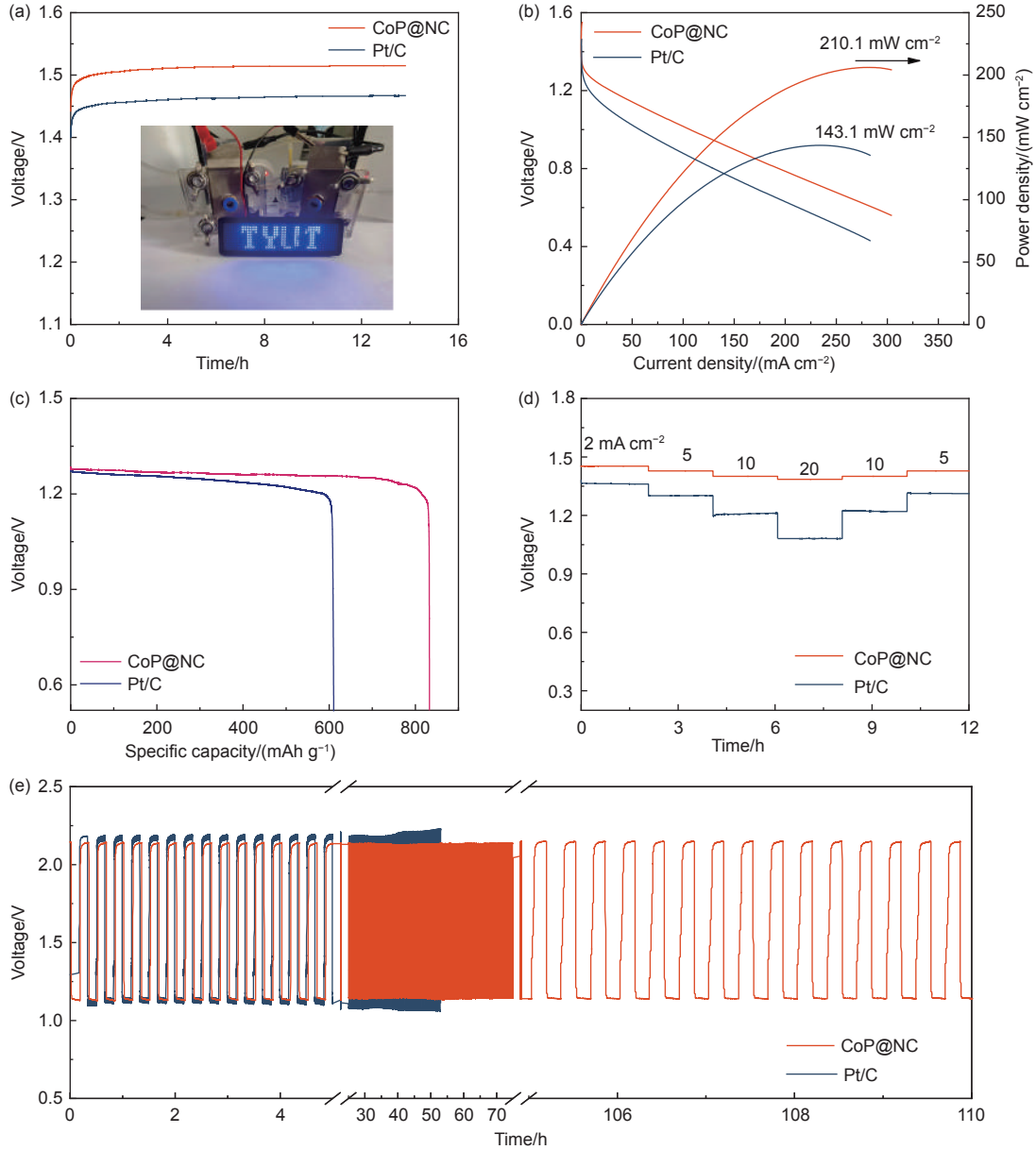

Fig. 4 (a) Open-circuit voltage profile of ZABs under alkaline solution assembled using CoP@NC and Pt/C catalysts as air cathode materials. (Inset) Photograph of connecting two ZABs lighting up a LED. (b) Polarization curves and power density curves of the of ZABs of the CoP@NC and Pt/C catalysts. (c) Discharging capacity curves normalized by the consumed Zn of CoP@NC and Pt/C . (d) Rate performance of ZABs with CoP@NC and Pt/C (20%) as air cathode at 2-20 mA cm^{-2}, respectively. (e) Charge-discharge cycle curves of ZABs using CoP@NC and Pt/C catalysts

fully demonstrates that CoP@NC not only has excellent catalytic efficiency and durability, but also has the potential to be employed as air positive material for a ZAB, which has a promising prospect in the field of advanced energy storage.

4 Conclusion

The hierarchical porous carbon with controlled size and reasonable microporous/mesoporous ratio was used as the carrier, and then the well dispersed CoP nanoparticles encapsulated in the carbon shell were successfully immobilized on the support. The achieved CoP@NC catalyst shows a boosted ORR performance with a $E_{1/2}$ of 0.92 V under alkaline conditions. The remarkable ORR activity of CoP@NC is mainly due to the numerous CoP active sites evenly embedded in the porous carbon framework and the strong electronic coupling between carbon matrix and the CoP nanoparticles. The CoP@NC electrocatalyst

assembled as a cathode catalyst for Zn-air battery has a high open-circuit voltage, exceptional power density and an excellent stability. This study provides a guidance for the design of novel noble metal-free catalysts with potential applications in zinc-air batteries.

Acknowledgements

This work was supported by the National Natural Science Foundation of China (12305332), Natural Science Foundation of Shanxi Province (202203021221089), Science and Technology Innovation Talent Team Project of Shanxi Province (202304051001010), Scientific and Technological Innovation Programs of Higher Education Institutions in Shanxi (2019L0253), and Program for the Innovative Talents of Higher Education Institutions of Shanxi (PTIT).

References

[1] Wang Q, Liang H, Zhou J, et al. Boosting oxygen reduction catalysis by introducing Fe bridging atoms between Pt nanoparticles and N-doped graphene[J]. Chemical Engineering Journal, 2023, 467: 143482.

[2] Zhang Y, Zhang H, Sha W, et al. N-doped graphene nanoribbons intertwined on 3D graphene skeleton as superior metal-free electrocatalyst for oxygen reduction[J]. Colloids and Surfaces A:Physicochemical and Engineering Aspects, 2022, 652: 129832.

[3] An F, Bao X Q, Deng X Y, et al. Carbon-based metal-free oxygen reduction reaction electrocatalysts: past, present and future[J]. New Carbon Materials, 2022, 37(2): 338-354.

[4] Shi J, Lin N, Lin H B, et al. A N-doped rice husk-based porous carbon as an electrocatalyst for the oxygen reduction reaction[J]. New Carbon Materials, 2020, 35(4): 401-409.

[5] Li H, Zhang H X, Yan X L, et al. Carbon-supported metal single atom catalysts[J]. New Carbon Materials, 2018, 33(1): 1-11.

[6] Song Y, Zhang T, Zhou G, et al. Cu nanoclusters on N-doped carbon nanotubes as efficient electrocatalyst for oxygen reduction reaction[J]. Applied Surface Science, 2022, 589: 153022.

[7] Li P, Wang H L. Recent advances in carbon-supported iron group electrocatalysts for the oxygen reduction reaction[J]. New Carbon Materials, 2021, 36(4): 665-682.

[8] Ren X P, Hu Q W, Ling F, et al. Mott-Schottky heterojunction formation between Co and $MoSe_2$ on carbon nanotubes for superior hydrogen evolution[J]. New Carbon Materials, 2023, 38(6): 1059-1069.

[9] Guo J, Mao Z, Yan X, et al. Ultrasmall tungsten carbide catalysts stabilized in graphitic layers for high-performance oxygen reduction reaction[J]. Nano Energy, 2016, 28: 261-268.

[10] Tu H, Zhang H, Song Y, et al. Electronic asymmetry engineering of Fe—N—C electrocatalyst via adjacent carbon vacancy for boosting oxygen reduction reaction[J]. Advanced Science, 2023, 10(32): 2305194.

[11] Wang X R, Liu J Y, Liu Z W, et al. Identifying the key role of pyridinic-N—Co bonding in synergistic electrocatalysis for reversible ORR/OER[J]. Advanced Materials, 2018, 30(23): 1800005.

[12] Xu X X, Zhang N C, Wang J Y, et al. The synthesis of iron-nitrogen sites embedded in electrospun carbon nanofibers with an excellent oxygen reduction reaction activity in alkaline/acidic media[J]. New Carbon Materials, 2023, 38(1): 154-160.

[13] Zhang Y T, Li S Y, Zhang N N, et al. A carbon catalyst doped with Co and N derived from the metal-organic framework hybrid (ZIF-8@ZIF-67) for efficient oxygen reduction reaction[J]. New Carbon Materials, 2023, 38(1): 200-209.

[14] Zhang H, Zhang Z, Zhang Z, et al. Highly dispersed ultrasmall iron phthalocyanine molecule clusters confined by mesopore-rich N-doped hollow carbon nanospheres for efficient oxygen reduction reaction and Zn-air battery[J]. Chemical Engineering Journal, 2023, 469: 143996.

[15] Liu W, Hu E, Jiang H, et al. A highly active and stable hydrogen evolution catalyst based on pyrite-structured cobalt phosphosulfide[J]. Nature Communications, 2016, 7(1): 10771.

[16] He X F, Chang L B, Han P F, et al. Highly efficient Co−N−C electrocatalysts with a porous structure for the oxygen reduction reaction[J]. New Carbon Materials, 2023, 38(5): 976-988.

[17] Zhang J, Song L, Zhao C, et al. Co, N co-doped porous carbons as high-performance oxygen reduction electrocatalysts[J]. New Carbon Materials, 2021, 36(1): 209-218.

[18] Tang C, Titirici M M, Zhang Q. A review of nanocarbons in energy electrocatalysis: Multifunctional substrates and highly active sites[J]. Journal of Energy Chemistry, 2017, 26(6): 1077-1093.

[19] Li X, Jiang Q, Dou S, et al. ZIF-67-derived Co-NC@CoP-NC nanopolyhedra as an efficient bifunctional oxygen electrocatalyst[J]. Journal of Materials Chemistry A, 2016, 4(41): 15836-15840.

[20] Zhang D, Ding R, Tang Y, et al. Stable Co/N-doped carbon nanotubes as catalysts for oxygen reduction[J]. ACS Applied Nano Materials, 2022, 5(7): 10026-10035.

[21] Li M, Shi J, Xu B, et al. Size-controlled Co/CoO heterogeneous nanoparticles confined in N-doped mesoporous carbon for efficient oxygen reduction in zinc-air batteries[J]. Journal of Colloid and Interface Science, 2024, 653: 1317-1325.

[22] Liu H, Liu Z H, Zhang J Q, et al. Boron and nitrogen co-doped

carbon dots for boosting electrocatalytic oxygen reduction[J]. New Carbon Materials, 2021, 36(3): 585-593.

[23] Ye X W, Hu L B, Liu M C, et al. Improved oxygen reduction performance of a N, S co-doped graphene-like carbon prepared by a simple carbon bath method[J]. New Carbon Materials, 2020, 35(5): 531-539.

[24] Rao P, Wu D, Wang T J, et al. Single atomic cobalt electrocatalyst for efficient oxygen reduction reaction[J]. eScience, 2022, 2(4): 399-404.

[25] Shi Q, Liu Q, Ma Y, et al. High-performance trifunctional electrocatalysts based on FeCo/Co_2P Hybrid Nanoparticles for Zinc –air battery and self-powered overall water splitting[J]. Advanced Energy Materials, 2020, 10(10): 1903854.

[26] Zhu C, Zhao S, Fan Z, et al. Confinement of CoP nanoparticles in nitrogen-doped yolk-shell porous carbon polyhedron for ultrafast catalytic oxidation[J]. Advanced Functional Materials, 2020, 30(49): 2003947.

[27] Li Y, Dong Z, Jiao L. Multifunctional transition metal-based phosphides in energy-related electrocatalysis[J]. Advanced Energy Materials, 2020, 10(11): 1902104.

[28] Tang C, Wang B, Wang H F, et al. Defect engineering toward atomic Co－N_x－C in hierarchical graphene for rechargeable flexible solid Zn-air batteries[J]. Advanced Materials, 2017, 29(37): 1703185.

[29] Liu J, Guo Y, Fu X Z, et al. Strengthening absorption ability of Co–N–C as efficient bifunctional oxygen catalyst by modulating the d band center using MoC[J]. Green Energy & Environment, 2023, 8(2): 459-469.

[30] Lin Y, Yang L, Zhang Y, et al. Defective carbon–CoP nanoparticles hybrids with interfacial charges polarization for efficient bifunctional oxygen electrocatalysis[J]. Advanced Energy Materials, 2018, 8(18): 1703623.

[31] Liu J, Zhang C, Yuan S, et al. CoP-decorated N, P-doped necklace-like carbon for highly efficient oxygen reduction and Al-air batteries[J]. Chemical Engineering Journal, 2022, 428: 131326.

[32] Li J, Liu G, Liu B, et al. An extremely facile route to Co2P encased in N, P-codoped carbon layers: Highly efficient bifunctional electrocatalysts for ORR and OER[J]. International Journal of Hydrogen Energy, 2018, 43(3): 1365-1374.

[33] Wang Q, Fan Y, Wang K, et al. Hierarchical tubular structures composed of CoPx and carbon nanotubes: Highly effective electrocatalyst for oxygen reduction[J]. Carbon, 2018, 130: 241-249.

[34] Huang X, Xu X, Li C, et al. Vertical CoP nanoarray wrapped by N, P-doped carbon for hydrogen evolution reaction in both acidic and alkaline conditions[J]. Advanced Energy Materials, 2019, 9(22): 1803970.

[35] Akula S, Mooste M, Kozlova J, et al. Transition metal (Fe, Co, Mn, Cu) containing nitrogen-doped porous carbon as efficient oxygen reduction electrocatalysts for anion exchange membrane fuel cells[J]. Chemical Engineering Journal, 2023, 458: 141468.

[36] Li H, Li Q, Wen P, et al. Retracted: Colloidal cobalt phosphide nanocrystals as trifunctional electrocatalysts for overall water splitting powered by a Zinc-air battery[J]. Advanced Materials, 2018, 30(9): 1705796.

[37] Zhou G, Yan X, Zhang T, et al. MOFs-derived hierarchical porous carbon supported Co@NC nanocapsules for pH universal oxygen reduction reaction and Zn-air batteries[J]. Applied Surface Science, 2023, 621: 156906.

[38] Wang Y, Wu M, Li J, et al. In situ growth of CoP nanoparticles anchored on (N, P) co-doped porous carbon engineered by MOFs as advanced bifunctional oxygen catalyst for rechargeable Zn-air battery[J]. Journal of Materials Chemistry A, 2020, 8(36): 19043-19049.

[39] Fu G, Liu Y, Chen Y, et al. Robust N-doped carbon aerogels strongly coupled with iron–cobalt particles as efficient bifunctional catalysts for rechargeable Zn-air batteries[J]. Nanoscale, 2018, 10(42): 19937-19944.

[40] Liu W, Zhou Z, Li Z, et al. Cobalt phosphide embedded N-doped carbon nanopolyhedral as an efficient cathode electrocatalyst in microbial fuel cells[J]. Journal of Environmental Chemical Engineering, 2021, 9(1): 104582.

[41] Yang T, Wang Z, Li K, et al. Surface-oxidized cobalt phosphide used as high efficient electrocatalyst in activated carbon air-cathode microbial fuel cell[J]. Journal of Power Sources, 2017, 363: 87-94.

[42] Chen T, Ma J, Chen S, et al. Construction of heterostructured CoP/CN/Ni: Electron redistribution towards effective hydrogen generation and oxygen reduction[J]. Chemical Engineering Journal, 2021, 415: 129031.

[43] Chen J, Huang J, Wang H, et al. Phase-mediated cobalt phosphide with unique core-shell architecture serving as efficient and bifunctional electrocatalyst for hydrogen evolution and oxygen reduction reaction[J]. Chinese Chemical Letters, 2022, 33(8): 3752-3756.

[44] Liu B, Wang R, Yao Y, et al. Hollow-structured CoP nanotubes wrapped by N-doped carbon layer with interfacial charges polarization for efficiently boosting oxygen reduction/evolution reactions[J]. Chemical Engineering Journal, 2022, 431: 133238.

[45] Go H W, Nguyen T T, Ngo Q P, et al. Tailored heterojunction active sites for oxygen electrocatalyst promotion in Zinc-air batteries[J]. Small, 2023, 19(10): 2206341.

[46] Li M, Pan X, Jiang M, et al. Interface engineering of oxygen-vacancy-rich CoP/CeO_2 heterostructure boosts oxygen evolution reaction[J]. Chemical Engineering Journal, 2020, 395: 125160.